Cloudy-sky land surface temperature from VIIRS and MODIS satellite data using a surface energy balance-based method

Aolin Jia[a], Han Ma[b], Shunlin Liang[a,*], and Dongdong Wang[a]

[a] Department of Geographical Sciences, University of Maryland, College Park, MD, 20742, USA

[b] School of remote sensing and information engineering, Wuhan University, Wuhan, Hubei 430079, China

**Correspondence to*: Shunlin Liang (sliang@umd.edu)

Abstract

Land surface temperature (LST) has been effectively retrieved from thermal infrared (TIR) satellite measurements under clear-sky conditions. However, TIR satellite data are often severely contaminated by clouds, which cause spatiotemporal discontinuities and low retrieval accuracy in the LST products. Several solutions have been proposed to fill the “gaps”; however, a majority of these possess constraints. For example, fusion methods with microwave data suffer from coarse spatial resolution and diverse land cover types while spatial-temporal interpolation methods neglect cloudy cooling effects. We developed a novel method to estimate cloudy-sky LST from polar-orbiting satellite data based on the surface energy balance (SEB) principle. First, the hypothetical clear-sky LST of missing or likely cloud-contaminated pixels was reconstructed by assimilating high-quality satellite retrievals into a time-evolving model built from reanalysis data using a Kalman filter data assimilation algorithm. Second, clear-sky LST was hypothetically corrected by accounting for cloud cooling based on SEB theory. The proposed method was applied to Visible Infrared Imaging Radiometer Suite (VIIRS) and Moderate Resolution Imaging Spectroradiometer (MODIS) data, and further validated using ground measurements of fourteen sites from SURFRAD, BSRN, and AmeriFlux in 2013. VIIRS LST recovered from cloud gaps exhibited a root mean square error (RMSE) of 3.54 K, a bias of −0.36 K, R^2 of 0.94, and sample size (N) of 2,411, comparable to the accuracy of clear-sky LST products and cloudy-sky LST estimation from MODIS (RMSE of 3.69 K, bias of −0.45 K, R^2 of 0.93, and N of 2,398). Thus, the proposed method performs well across different sensors, seasons, and land cover types. The abnormal retrieval values caused by cloud contamination were also corrected in the proposed method. The overall accuracy was better than the downscaled cloudy-sky LST retrieved from passive microwave (PMW) observations and former SEB-based cloudy-sky LST estimation methods. Validation using time-series measurements showed that the all-sky LST time series, including both clear- and cloudy-sky retrievals, can capture realistic variability without sudden abruptions or discontinuities. RMSE values for the all-sky LST varied from 2.54 to 4.15 K at the fourteen sites. Spatially continuous LST maps over the Contiguous United States were compared with corresponding maps from PMW data in the winter and summer of 2018, exhibiting similar spatial patterns but with additional spatial details. Moreover, sensitivity analysis suggested that the reconstruction of clear-sky LST dominantly impacts the accuracy of cloudy-sky LST estimation. The proposed method can be potentially implemented in similar satellite sensors for global real-time production.

Keywords: land surface temperature, cloudy-sky, data assimilation, surface energy balance principle, VIIRS and MODIS

1. Introduction

By reflecting the state of exchange of energy and water at the surface-atmosphere interface, land surface temperature (LST) is an essential parameter in surface radiation and hydrological balances at regional and global scales (Chen and Liu, 2020; Li et al., 2013; Liang et al., 2019; Liang et al., 2010). LST has been extensively used in many applications, such as evapotranspiration estimation, drought prediction, and monitoring climate warming and environmental change (Hansen et al., 2010; Jia et al., 2020; Tomlinson et al., 2011; Xu et al., 2019). However, given the complexity and high heterogeneity of LST caused by topography, land cover, and soil type (Liu et al., 2006; Luyssaert et al., 2014), there is an urgent need to obtain spatiotemporally continuous LST data over large areas. Satellite remote sensing is the only feasible approach for mapping LST over the entire globe (Li et al., 2013; Liang, 2017; Wan and Li, 1997).

Satellite LST products are mostly derived from thermal infrared (TIR) observations, such as the Moderate Resolution Imaging Spectroradiometer (MODIS) (Wan, 2006; Zhou et al., 2018), Visible Infrared Imaging Radiometer Suite (VIIRS) (Islam et al., 2016), Landsat (Sobrino et al., 2004), Geostationary Operational Environmental Satellite (GOES)-R (Yu et al., 2008), and Advanced Very-High-Resolution Radiometer (AVHRR) (Liu et al., 2019). However, TIR ground signals cannot be observed under cloudy sky conditions, leading to null-value pixels in satellite-derived LST products affected by cloud coverage. Moreover, some retrieved pixels may still be contaminated by clouds and have low accuracy. These spatially and temporally incomplete LST products significantly restrict their subsequent application at regional and global scales. Therefore, eliminating cloud contamination and filling cloud gaps in LST products are highly prioritized in relevant research.

A number of methods have been developed to estimate LST under cloudy sky conditions; they can be mainly divided into four categories: passive microwave (PMW) data-based, spatial-temporal interpolation, machine learning, and surface energy balance (SEB) methods.

PMW remotely sensed data can penetrate clouds and have been considered an important solution for cloudy-sky LST estimations. Many PMW LST algorithms have been proposed, which can be grouped into three classes: empirical (Chen et al., 2011; Holmes et al., 2009; Owe and Van De Griend, 2001; Zhou et al., 2015), semiempirical (Chen et al., 2011; Fily et al., 2003; Gao et al., 2007), and physical (Njoku and Li, 1999; Wen et al., 2003; Weng and Grody, 1998) methods. The achieved accuracies vary by up to 6 K for the global LST diurnal cycle (Dash et al., 2002). However, PMW observations remain limited owing to a number of issues. First, the low rate of change in the PMW radiance with a high variance in surface emissivity causes difficulties in estimating LST with acceptable accuracy (Zhang et al., 2019a). Furthermore, microwave data with a coarse spatial resolution fail to capture spatial details. Finally, temperature retrieval from PMW observations yields subsurface temperature, which is different from the skin temperature retrieved from TIR data (Galantowicz et al., 2011). Recent studies have attempted to generate all-weather LST by fusing PMW with TIR observations at regional scales (Duan et al., 2017; Kou et al., 2016; Xu and Cheng, 2021; Zhang et al., 2019b; Zhang et al., 2020). However, global surface and atmospheric conditions are complex, and statistical parameters cannot be easily applied. Moreover, PMW data still contain large swath gaps in the middle and low latitudes. Therefore, downscaling and fusion methods are not practical at a global scale.

Multiple spatial-temporal interpolation methods have been proposed to resolve problems caused by cloud contamination. Basic spatial interpolation methods include inverse distance weighting (IDW), kriging interpolation (Neteler, 2010; Westermann et al., 2011), and representative temporal reconstruction methods using the harmonic analysis of time series (HANTS) algorithm (Xu and Shen, 2013), temporal Fourier analysis, and asymmetric Gaussian function fitting method. Spatial-temporal interpolation methods treat spatiotemporally neighboring pixels as references. Nevertheless, the interpolation accuracy relies on the distributions of the pixels and the surface homogeneity. Therefore, interpolation methods usually have a smoothing effect, and extreme LST variation may not be well captured. Moreover, climate factors are not considered, and statistics-based interpolations do not follow the physical relationships among basic environmental variables. For example, clouds usually have negative radiative forcing at the surface level while the cloudy-sky LST is lower than that of clear-sky cases. Theoretically, interpolated LST is hypothetical clear-sky LST rather than cloudy-sky LST.

Considering that simple statistical models can only be utilized under limited conditions, machine learning has recently shown an extraordinary ability to capture surface complexity and reconstruct missing remotely sensed data (Das and Ghosh, 2017; Nogueira et al., 2018; Zhang et al., 2016; Zhang et al., 2018). Rao et al. (2019) estimated the all-weather surface air temperature over the Tibetan Plateau using the Cubist model. However, this requires spatiotemporally continuous input data. Wu et al. (2019) employed conventional neural networks to reconstruct geostationary satellite LST. Nevertheless, this model is based on statistical information with no constraints from environmental factors. Zhao and Duan (2020) estimated cloudy-sky LST by implementing random forest, incorporating training data from clear-sky days. As the accuracy is comparable to the reanalysis data, further assessment using site observations is needed. Fu et al. (2019) coupled the random forest model with the weather research and forecasting (WRF) model and retrieved urban LST under cloudy conditions. The accuracy varied from 1.0 to 9.0 K across different land cover. In general, machine learning methods rely heavily on the sampling amount and quality of input; if sample representativeness is regionally limited, the model cannot be used for large areas, and it is difficult to collect globally distributed training data. Moreover, machine learning remains statistics-based and offers no clear physical interpretations, making uncertainty analysis unfeasible. Therefore, a practical physical method for estimating cloudy-sky LST is required.

Jin (2000) proposed a neighboring-pixel (NP) approach to estimate the LST of cloudy pixels based on SEB theory. This approach mainly includes two steps: (1) reconstructing clear-sky LST for a target cloudy pixel using reference information from spatially or temporally neighboring clear-sky LST, and (2) correcting the reconstructed clear-sky LST to the real cloudy-sky LST by adding the cloud effect of the LST estimated from all-sky downward shortwave radiation (DSR) with SEB equations (Liang, 2004). Near-surface meteorological observations (air temperature and wind) are therefore required. As the SEB method is physically based and the driving factors (such as the DSR) are available in all weather conditions, it has significant potential for cloudy-sky LST estimations. Following this approach, Lu et al. (2011) estimated cloudy-sky LST by exploiting the temporal domain from geostationary Meteosat Second Generation. Yu et al. (2014) applied this method to the MODIS LST product. However, ground-measured environmental variables are still required, yielding difficulties in implementing this method for ungauged or poorly gauged regions. Zeng et al. (2018) revised the method to use vegetation indices for neighboring similar pixel selection. They also obtained regional parameters from clear-sky neighboring pixels and applied them to the cloudy effect correction. Thus, no ground meteorological measurements were required in the algorithm, allowing implementation at large spatial scales. Such vegetation index-based methods were also used by Yang et al. (2019). However, spatially neighboring pixels are not always available if clouds cover large areas; searching for similar neighboring pixels is time-consuming. The linear relationships between vegetation indices and LST are not reliable (Sun and Kafatos, 2007; Yuan et al., 2020), especially in non-growing seasons. This is because vegetation index values for the entire image can be low while the LST still has spatial variance affected by soil moisture and terrain. Therefore, a more feasible SEB-based cloudy-sky LST estimation method that can be applied at a large spatial scale is necessary.

Moreover, previous research has predominantly focused on cloud gap filling, whereas the reconstruction of some retrieved, but cloud-contaminated pixels has been rarely discussed (Yang et al., 2019). These pixels may cause uncertainty while noted as contextual information in previous studies. Compared with polar-orbiting satellite products, reanalysis data have the advantage of spatiotemporal continuity (Jia et al., 2018; Zhang et al., 2021). As reanalysis data are upgraded to a new generation, they attain a higher accuracy and resolution compared with former generations, providing a new possibility to combine them with satellite retrievals to estimate cloudy-sky LST and remove cloud contamination (Long et al., 2020; Zhang et al., 2021).

The objective of this study was to develop a generic SEB-based physical method for estimating cloudy-sky LST from different polar-orbiting satellite data (e.g., MODIS and VIIRS). We first reconstructed hypothetical clear-sky LST of cloudy pixels and likely cloud-contaminated pixels by assimilating high-quality satellite retrieved LST into a time-evolving model built from the European Centre for Medium-Range Weather Forecasts (ECMWF) Reanalysis 5th Generation (ERA5) reanalysis data (Hersbach et al., 2020) using a Kalman filter (KF) algorithm. Furthermore, we estimated the LST differences resulting from cloud impacts according to SEB theory. This method is an extension of our recently developed simultaneous retrieval algorithm (Ma et al., 2020; Ma et al., 2017; Ma et al., 2018; Shi et al., 2017), which simultaneously inverts multiple environmental variables with physical consistency from optical-thermal top of atmosphere (TOA) remote sensing observations.

2. Methods and Data

2.1 Flowchart description

The proposed method comprises two steps (Figure 1). The first step was to construct the hypothetical clear-sky LST for cloud-contaminated and cloudy pixels. Modeled clear-sky LST over one year from reanalysis data was calibrated using satellite LST retrievals through a KF, and the hypothetical clear-sky LST was reconstructed for missing days or days likely contaminated by clouds. The second step was to estimate the net effect of clouds on the hypothetical clear-sky LST. The cloud effect was calculated from the ground heat flux, which is an energy-partitioned component of the net radiation. Further, the cloud was superposed to the reconstructed LST for the cloudy days.

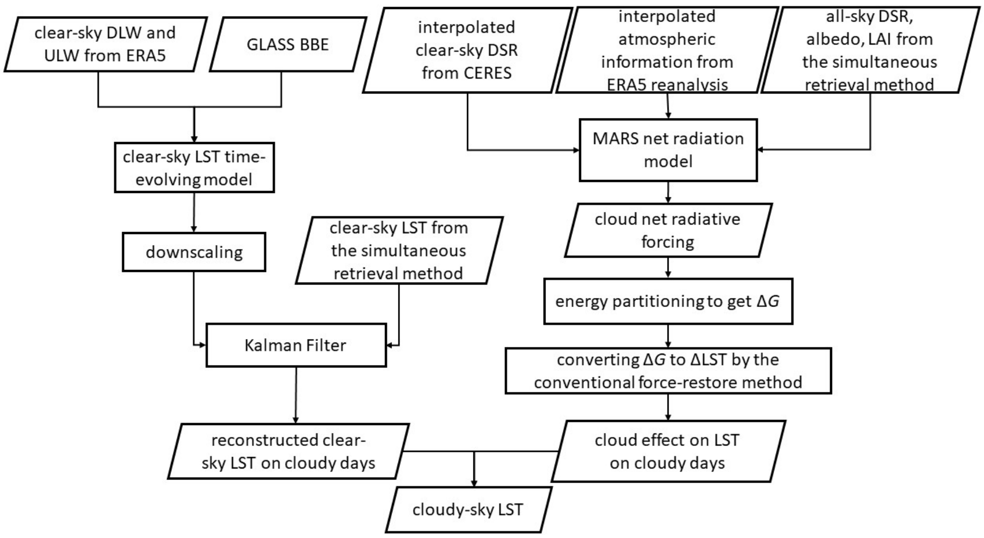

Figure 1. Flowchart of the proposed cloudy-sky land surface temperature (LST) estimation method, where DLW and ULW are the downward and upward longwave radiation, respectively,

BBE is the broadband emissivity, DSR is the downward shortwave radiation, LAI is the leaf area index, and ΔG and ΔLST are the cloud effect on the ground heat and LST, respectively.

First, the hypothetically clear-sky LST was reconstructed for all likely cloud-contaminated and cloudy days. For a target LST product pixel, corresponding clear-sky LST series were used for building a clear-sky LST annual dynamic model (a time-evolving model), computed from the clear-sky longwave radiation of the ERA5 reanalysis data. This model predicts the clear-sky surface longwave radiation over one year. Although the clear-sky LST is estimated from clear-sky longwave radiation components with surface broadband emissivity (Equation 1), it does not respond to the ERA5 skin temperature, which is an all-weather surface temperature. Clear-sky longwave radiation components are simulated for the same temperature and humidity atmospheric conditions as the corresponding real condition while assuming the absence of clouds.

The first estimation of the annual temporal profile of the clear-sky LST was obtained after spatial downscaling. However, the dynamic model, built from the reanalysis datasets, may not provide accurate predictions due to the limitations in the downscaling method and model parameterization. To increase the prediction accuracy and calibrate the dynamic model, clear-sky LST retrievals of the pixel over one year were assimilated by the KF to the annual dynamic model. Furthermore, a hypothetically clear-sky LST was reconstructed for all cloudy days of the year. Sections 2.2 and 2.3 present further details on this step.

Secondly, the cloud effect was superposed on the reconstructed clear-sky LST based on SEB theory. Theoretical clear-sky DSR in targeted cloudy days and corresponding realistic cloudy-sky DSR from the simultaneous retrieval were used as the basic inputs of a trained multivariate adaptive regression spline (MARS) model (Jiang et al., 2016) to estimate the cloud net radiative forcing on cloudy days. After partitioning the cloud net radiative forcing to the ground heat component, the cloud effect of the LST was estimated based on the conventional force-restore method. Section 2.4 presents details on the second step.

2.2 Clear-sky LST annual dynamic model

The dynamic model was used to predict the hypothetical clear-sky LST for each cloud-affected day over one year. The ERA5 officially publishes spatiotemporally continuous clear-sky surface downward and upward longwave radiation (DLW and ULW, respectively), which were employed to estimate the clear-sky LST series as follows:

$$LST = \sqrt[4]{\frac{\mathrm{ULW}-(1-\varepsilon_s)\mathrm{DLW}}{\varepsilon_s \sigma}}, \tag{1}$$

where ε_s is the broadband emissivity (BBE), which can be obtained from the Global Land Surface Satellite (GLASS) BBE product (Cheng et al., 2015). However, the modeled clear-sky LST has a coarser spatial resolution. By following Duan et al. (2017), we applied a practical downscaling method to obtain the first estimate of the clear-sky LST series as follows:

$$T_f = T_c + TLR \times (H_i - H_m) + K \times (V_i - V_m), \tag{2}$$

where T_f is the downscaled LST at a resolution (0.01°); T_c is the LST at the original coarse spatial resolution (0.25 °); the second component on the right is the correction for elevation: *TLR* is the temperature lapse rate, which is defined as the rate of decrease in temperature with altitude, whose average is 6.5 K/km (Minder et al., 2010); and H_i is surface elevation of the *i*th pixel at the satellite pixel scale while H_m is the averaged surface elevation of the modeled pixel. We added the third component for correcting the vegetation influence, *K*, which is the linear regression slope between the satellite-derived 1-km clear-sky LST and the corresponding LAI under the target coarse model pixel within 8 days. Furthermore, V_i and V_m are the LAI values of the *i*th pixel at the satellite pixel scale and averaged model pixel scale, respectively. The third component was not included if the *p*-value of the regression was larger than 0.05 because the relationship between the LST and vegetation coverage may not be reliable, especially during the non-growing season or sparsely vegetated areas. Such a downscaling method was also used for the all-sky PMW LST in the analysis.

Therefore, the downscaled continuous clear-sky LST series was treated as the corresponding annual dynamic model. The annual dynamic model is a time-evolving model that can be described mathematically as follows:

$$LST_t = F_t \times LST_{t-1}, \tag{3}$$

$$F_t = 1 + \frac{1}{Z_t + \delta} \times \frac{dZ_t}{dt}, \tag{4}$$

where Z_t represents the difference in the clear-sky LST at day t and day $t - 1$, which is the temporal profile from the LST dynamic model over one year, and δ = 0.01 avoids a null denominator. As the clear-sky LST is computed from the ERA5 modeled longwave radiation with uncertainty, spatially downscaling and assimilating satellite LST retrievals with high accuracy is necessary to calibrate the annual dynamic model prediction. The ERA5 clear-sky LST was extracted based on the passing time of the satellite each day. Only the estimated clear-sky LST series, rather than the ERA5 all-sky skin temperature, were employed because a more accurate cloud effect estimated from the satellite products was superimposed in subsequent steps.

2.3 Kalman Filter

Owing to the modeling uncertainty, there are differences between the real LST variation and prediction of the dynamic model built for a target pixel. Therefore, when a newly retrieved

LST is available, it is assimilated into the dynamic model by the KF to fit the real condition. Such a frame is suitable for use as future real-time all-sky LST production. The KF calculates the weighted average of the dynamic model result and real-time retrievals according to the criterion of the minimum mean square error (Bishop and Welch, 2001). The prediction (Equations 5 – 7) process was as follows:

$$z_k = x_k + v_k, \tag{5}$$

$$\hat{x}^-{}_k = A\hat{x}_{k-1} + \omega_{k-1}, \tag{6}$$

$$P^-{}_k = AP_{k-1}A^T + Q, \tag{7}$$

where, z_k, the clear-sky LST obtained from satellite observations at day k, is represented by the retrieved LST value, x_k, with retrieval error, v_k (covariance is R), $\hat{x}^-{}_k$ is the prior estimate of the clear-sky LST directly from the annual dynamic model, A, and ω_{k-1} is the model error with a covariance of Q.

We determined R via the nominal accuracy in the quality control (QC) of the LST product: if the nominal accuracy (bit 14 & 15) was marked as excellent, R = 1; if it is good, R = 4; if it is marginal, R = 9; and if it is poor, R = 16. Therefore, R was adjusted as new retrievals were obtained to meet the spatiotemporal variability in the LST retrieval accuracy. The initial value of Q was equal to the squared ERA RMSE, where ERA RMSE is the RMSE of ERA5 clear-sky LST, calculated by comparing samples on clear days with satellite retrievals over one year. Only the high-quality retrieved LST (not contaminated by clouds) was assimilated into the dynamic model, and the likely contaminated samples were marked by a cloud flag (thin cirrus or a pixel within two pixels of the nearest cloud), with poor nominal accuracy (Duan et al., 2017). These retrieved, but likely contaminated, cases were reconstructed and validated separately to demonstrate the feasibility of the proposed method at different cloud disturbance conditions. The LST of the VIIRS simultaneous retrieval refers to the QC from the VNP21 product.

$P^{-}{}_{k}$ is the prior covariance estimate after model prediction. The second step corrected the modeling using new observations (Equations 8 – 10):

$$\hat{x}_k = \hat{x}^{-}{}_{k} + K_k(z_k - \hat{x}^{-}{}_{k}), \tag{8}$$

$$P_k = (I - K_k)P^{-}{}_{k}, \tag{9}$$

$$K_k = P^{-}{}_{k}(P^{-}{}_{k} + R)^{-1}. \tag{10}$$

The correction part included the final clear-sky LST estimation ($\hat{x}_k$) corrected from the $\hat{x}^{-}{}_{k}$ via the Kalman Gain (K_k); based on the difference between the model prediction and LST retrieval, the final output covariance was P_k. K_k is the combination of $P^{-}{}_{k}$ and R, which indicates that as the retrieval uncertainty, R, increases, K_k decreases, resulting in fewer corrections for $\hat{x}^{-}{}_{k}$, predicted by the dynamic model. By evolving the KF, the reconstruction of the clear-sky LST in a time-series can be calculated and the prediction uncertainty can be updated continuously.

2.4 SEB-based method

After clear-sky LST (T_{clear}) construction, the correction of the cloud effect (ΔT_s), estimated from R_n cloud radiative forcing, was added to obtain the real cloudy-sky LST (T_{cloud}):

$$T_{cloud} = T_{clear} + \Delta T_s, \tag{11}$$

where ΔT_s can be derived using SEB theory, which is expressed as follows:

$$R_n = S_n + L_n = G + LE + H, \tag{12}$$

where R_n is the balance of the net shortwave radiation (S_n) and net longwave radiation (L_n). Moreover, R_n is also the energy source of ground heat (*G*), latent heat (*LE*), and sensible heat (*H*).

To calculate the cloud effect of the LST, we must quantify the ground heat, *G*, which is the energy partitioned component, using the Land Surface Analysis Satellite Application Facilities (LSA-SAFs) ET algorithm (Arboleda et al., 2017) as follows:

$$G = \beta R_n, \tag{13}$$

$$\beta = 0.5exp(-2.13(0.88 - 0.78exp(-0.6LAI))), \tag{14}$$

where $\beta = 0.15$, 0.05, and 0.10 for rocks, snow, and inland water, respectively. Based on the conventional force-restore method, *G* can be also represented as follows (Jin and Dickinson, 2000):

$$G = k_g \frac{\partial T}{\Delta Z} = k_g \frac{T_s - T_d}{\Delta Z}, \tag{15}$$

where k_g is the thermal conductivity of the ground soil (W m^{-1} K^{-1}) and ΔZ is the depth of the subsurface layer (usually set as 0.1 m). Considering that the subsurface layer temperature, T_d, is significantly less sensitive than the LST (T_s) to the DSR, equation (15) can be modified as follows:

$$\frac{\partial G}{\partial T_s} = \frac{\partial}{\partial T_s}\left[k_g \frac{T_s - T_d}{\Delta Z}\right] \approx \frac{k_g}{\Delta Z}, \tag{16}$$

Therefore, after quantifying ΔG from the partitioned energy of the cloudy net radiative forcing, the cloud effect correction (ΔT_s) can be computed if ΔG, ΔZ, and k_g are known.

Following Zeng et al. (2018), we computed k_g from neighboring clear-sky days and applied it to cloudy days in the same pixel. First, the differences of the clear-sky LST for any paired days in a month were calculated. For these paired clear-sky days, ΔG can be directly calculated. By obtaining ΔG and ΔLST on clear-sky days, the k_g of all paired days can be computed (Equation 16); the monthly median k_g was used in this study to avoid extreme values caused by small temperatures or ground heat differences. Previous studies usually implemented a constant k_g for a specific soil type (Yu et al., 2014; Zhang et al., 2015) while the monthly k_g was used to reflect the impact of changes in the soil moisture.

Therefore, this section introduces a SEB-based method for estimating cloud radiative forcing. The essential theory relies on the relationship between the ground heat flux and LST (Equations 15 and 16) while assuming that the in-depth soil temperature remains stable. The ground heat flux was parameterized by the all-sky LAI and R_n, which can be directly obtained from the simultaneous retrieval method or current operational satellite products.

2.5 Daytime R_n estimation

As the longwave radiation components could not be obtained directly, we developed and trained the MARS model to estimate R_n from shortwave radiation components in the daytime. Based on previous studies (Jiang et al., 2016; Jiang et al., 2015), the daytime R_n can be estimated from the DSR, albedo, and other meteorological variables (e.g., the 2-m air temperature and total column water vapor) using the MARS model. To train the R_n model, training samples were extracted from the ERA5 records at 13:00 LT. MARS was only employed to duplicate the parameterization of the ERA5 R_n; we did not create a new R_n algorithm. Specifically, 600 locations were randomly selected over global land. Half of the samples were used for R_n model training (sampling in 2011–2012) while the remaining samples were used for validating MARS prediction accuracy (in 2013) by comparing the output with the ERA5 noon R_n. Figure 2 shows the training and prediction validation results.

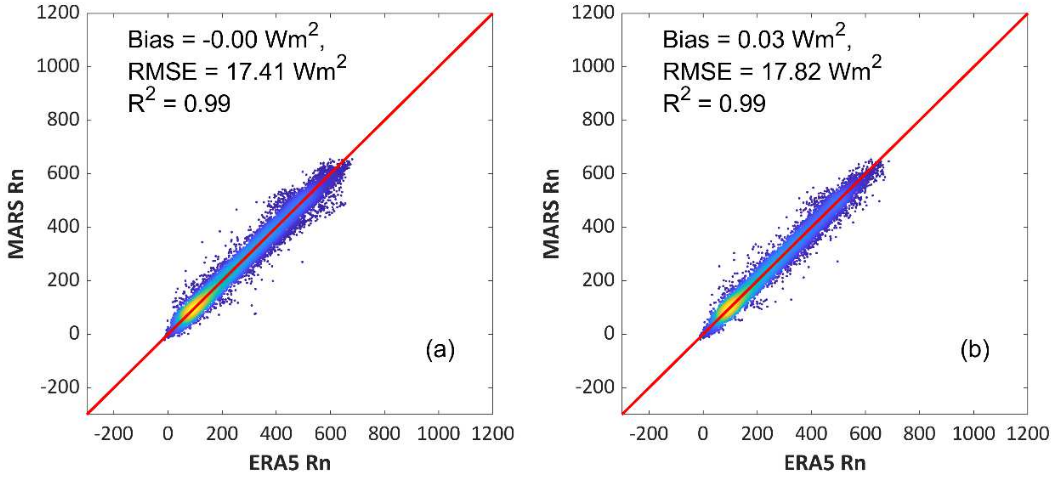

Figure 2. Validation of the multivariate adaptive regression splines (MARS) modeled R_n by comparison with the ERA5 R_n in terms of the (a) training accuracy and (b) prediction accuracy.

The training accuracy of the MARS R_n was 17.41 W m^{-2} with no bias while the prediction accuracy was 17.82 W m^{-2} with a bias of 0.03 W m^{-2}. The training and validation samples are location and time-independent; thus, the model had no overfitting issue. Further, the relative accuracy of the prediction was < 3 %, confirming that MARS can effectively duplicate the parametrization of the ERA5 R_n. The final inputs of the MARS model in this study included surface environmental variables (DSR, albedo, leaf area index [LAI], and clear index [DSR divided by the TOA DSR]) derived from the simultaneous retrieval, and atmospheric information (air temperature and total column water vapor) obtained from the ERA5, which were bilinearly interpolated. All previous cloudy-sky LST estimations based on SEB theory used the linear relationship to convert DSR to heat fluxes (Lu et al., 2011; Yu et al., 2014; Zeng et al., 2018), which introduced more uncertainties and coefficients that were not feasible at a large scale; in comparison, this method reduced the uncertainty of the surface energy balance estimation.

2.6 PMW LST calculation

In order to compare the validation statistics and assess the all-sky LST imagery recovery of the proposed method, PMW observations were used to obtain all-sky LST for comparison. The Four-Channel Algorithm (Mao et al., 2007) was employed to convert the brightness temperature (BT) to the LST by combining the PMW observations at different frequencies. The BT difference in the 36.5 and 23.8 GHz channels in vertical polarization was used to minimize the influence of atmospheric water vapor; T36.5V–T18.7H compensates for the influence of surface water while T89V decreases the average influence of the atmosphere (Sun et al., 2019). This can be expressed mathematically as follows:

$$LST = B_0 + B_1 T_{36.5V} + B_2(T_{36.5V} - T_{23.8V}) + B_3(T_{36.5V} - T_{18.7H}) + B_4 T_{89V}, \qquad (16)$$

where T represents the BTs and the subscripts denote frequencies in GHz for different bands; B_0–B_4 are regression coefficients obtained by the regression of the PMW BTs with the aggregated TIR LST on clear-sky days, further applied to the cloudy day cases. PMW BTs have a coarser spatial resolution of 0.1°. Moreover, TIR LST data were converted to lat/lon coordinates and aggregated to 0.1 ° only when 95 % of the 1-km pixels were retrieved in each aggregation group.

2.7 Data

In this study, we employed the clear-sky LST from VIIRS using the simultaneous retrieval method; the ERA5 clear-sky LST series was used for building the LST annual dynamic model. To demonstrate its feasibility with other polar-orbiting satellites, MODIS LST (MYD21) was also included. Fourteen ground sites from the Surface Radiation (SURFRAD) network, Baseline Surface Radiation Network (BSRN), and AmeriFlux were used for validation. Cloudy-sky LST, estimated from Advanced Microwave Scanning Radiometer 2 (AMSR2) microwave observations, were utilized for comparison. Further details of the data are given below; Tables 1 and 2 list the metadata.

2.7.1 Satellite data

The satellite products used in this study included outputs of the VIIRS simultaneous retrieval, LST products from the MODIS and VIIRS operational products, surface radiation components from the CERES products, auxiliary variables from the GLASS, and microwave observations from AMSR2. Table 1 summarizes the information and usages.

The MODIS and VIIRS clear-sky LST values can be obtained from the MODIS and VIIRS LST products; however, LST estimated using a simultaneous retrieval method provides a more accurate LST estimation. Ma et al. (2017) developed a simultaneous retrieval scheme to estimate a suite of parameters from both MODIS VNIR and thermal-infrared (IR) bands, based on a unified optical-thermal soil-canopy-leaf (PROSPECT + 4 SAIL) radiative transfer model, and an ensemble KF assimilation framework. The LAI was first determined by data assimilation and was then treated as a basic input parameter to produce the Fraction of Absorbed Photosynthetically Active Radiation (FAPAR), surface albedo, and land surface spectral emissivity (LSE). The ECOSTRESS spectral library (for twelve soil types) and UCSB spectral library (five leaf types) were employed. VIIRS directly observes the radiance at five middle infrared (MIR) and TIR bands, which was corrected to surface radiance using the satellite sounder product from the atmospheric infrared sounder (AIRS). With the determined spectral emissivity, the optimized LST can be determined by comparing the MIR–TIR surface radiances from the observations and calculations of the LSE and candidate LST. This method has been applied to VIIRS data (Ma et al., 2018), where the accuracy of the retrieved clear-sky LST was

~3 K higher than the VIIRS LST product. Further, a simultaneous retrieval scheme was revised, and an optimization method was used to assimilate the TOA observations to constrain the coupled model prediction. The DSR, LAI, albedo, LSE, and LST can be retrieved together (Ma et al., 2020). The accuracy of the instantaneous DSR can reach 102.9 W m^{-2}, which is better than the operational DSR products. This study applied the latest simultaneous retrieval scheme to the TOA VIIRS data from 2013 at 14 sites. The retrieved clear-sky LST was the basic input of the clear-sky LST reconstruction step. Furthermore, the instantaneous all-sky DSR, LAI, and albedo were included in the cloudy effect correction step. The clear-sky LST of MYD21 (Hulley et al., 2016) was employed to show that the proposed method is sensor independent and can be directly applied to different polar orbiting satellites during the daytime. The basic input for the MYD21 cloudy-sky LST was the same as the VIIRS but was accordingly extracted based on the MYD passing time. The DSR was converted to match the MYD21 passing time based on the time difference of the two satellites and the daily diurnal profile of DSR variation. The time profile was directly obtained from the spline-interpolated CERES SYN1deg-1hour product.

For cloudy-sky LST mapping, we used the all-sky DSR from the MODIS 3-h downward shortwave radiation (MCD18) product (Wang et al., 2020). The 3-h MCD18 was interpolated by a cosine function to obtain the noon all-sky DSR. The chosen year was 2018 because the newest MCD18 version was temporarily available. Eleven tiles, covering the Contiguous United States (CONUS), as well as from the VIIRS operational LST product (VNP21), were used. Other surface variables (such as the LAI and BBE), required for image recovery, were obtained from the GLASS all-sky product suites (Liang et al., 2014; Liang et al., 2013; Liu et al., 2013; Xiao et al., 2016).

To calculate the cloud net radiative forcing, the spline-interpolated clear-sky DSR series was extracted from the CERES SYN1deg-1hour clear-sky surface radiation products (Kato et al., 2018). The CERES SYN1deg products were retrieved from a combination of polar satellites (Terra + Aqua) with geostationary satellites (Loeb et al., 2018), which are based on the Fu-Liou radiative transfer theory (Fu et al., 1997). CERES provides daily theoretical 1° hourly clear-sky radiation products, which were estimated from all-weather radiation products by removing the cloudy impact; related cloud parameters were retrieved from multiple data sources, including microwave sensors (CERES_Team, 2013). The clear-sky DSR usually has limited spatial variability; thus, we directly used the bilinear interpolation to match the spatial scale and a spline interpolation to the diurnal profile to extract the clear-sky DSR at the VIIRS or MODIS passing time.

To compare the validation accuracy and assess the estimated cloudy-sky spatial pattern, PMW observations were used for calculating the all-sky LST. The AMSR2, onboard the GCOM-W1 satellite, is used for measuring PMW from Earth. The passing time is 13:30 LT, which is similar to the National Polar-orbiting Partnership (NPP) and Aqua satellites. It observes MW radiation from Earth's surface at seven frequencies (6.9, 7.3, 10.7, 18.7, 23.8, 36.5, and 89 GHz) in horizontal and vertical polarizations (Imaoka et al., 2010); we used 18.7, 23.8, 36.5, and 89 GHz at level 2A brightness temperatures to calculate the LST.

2.7.2 Reanalysis data

ERA5 provided the clear-sky longwave radiation components for building the LST annual dynamic model (Hersbach et al., 2020). Clear-sky longwave radiation components were simulated for the same temperature and humidity atmospheric conditions as the corresponding real condition (clouds included) while assuming that the clouds were absent. The clear-sky LST series utilized in this study can provide LST changes caused by local atmospheric variation or weather conditions without cloud forcing. The R_n MARS model requires the ERA5 samples for training and validation. The required variables for MARS training include the DSR, albedo, LAI, 2-m air temperature, total column water vapor, and R_n. The air temperature and total column water vapor are involved because they are the basic parameters of the atmospheric profiles (Wan and Li, 1997). The MARS R_n model is built from global land ERA5 samples to duplicate its R_n parameterization. We followed Jiang et al. (2016) and did not aim to propose a new R_n estimation method. The air temperature and total column water vapor were bilinearly interpolated while being utilized for satellite pixels.

Table 1. Metadata for the gridded satellite and reanalysis data.

Product	Variable	Time-span	Spatial resolution	Temporal resolution	Usage
ERA5	clear-sky DLW, ULW	2013, 2018	0.25 °	hourly	clear-sky LST dynamic model
GLASS	BBE	2013, 2018	1 km	daily	LST calculation from ULW & DLW
GMTED2010	DEM	2013, 2018	1 km	annual	LST downscaling
simultaneous retrieval method	clear-sky LST	2013	1 km	instantaneous	VIIRS hypothetical clear-sky LST reconstruction

MYD21	clear-sky LST	2013	1 km	instantaneous	MODIS hypothetical clear-sky LST reconstruction
ERA5	Air temperature, total water vapor, DSR, albedo, DLW, and ULW	2011–2013	0.25 °	hourly	MARS R_n modeling
simultaneous retrieval method	DSR	2013	1 km	instantaneous	cloud effect calculation
CERES	clear-sky DSR	2013, 2018	1°	hourly	cloud effect calculation
simultaneous retrieval method	albedo	2013	1 km	instantaneous	cloud effect calculation
simultaneous retrieval method	LAI	2013	1 km	daily	cloud effect calculation
MCD18A1	DSR	2018	1 km	3-hourly	all-sky LST mapping
VNP21	clear-sky	2018	1 km	instantaneous	all-sky LST mapping

	LST				
GLASS	albedo	2018	1 km	daily	all-sky LST mapping
GLASS	LAI	2013, 2018	1 km	daily	downscaling and all-sky LST mapping
AMSR2	PMW BT	2018	10 km	instantaneous	all-sky LST spatial comparison

*Data references are in the text and download sources are listed in the Acknowledgements.

2.7.3 Ground *in situ* measurements

Ground-observed LST for different surface types and climate regions was necessary to assess the proposed algorithm. 14 ground sites from SURFRAD, BSRN, and AmeriFlux were utilized for cloudy-sky LST validation. Established in 1993, SURFRAD was designed to support climate research with accurate, continuous, and long-term measurements of the surface radiation budget over the United States (Augustine et al., 2000). It has been widely used for LST validation (Li et al., 2013; Wang and Liang, 2009). BSRN (Ohmura et al., 1998) is a network that collects globally distributed sites from different projects. It has been in operation for one of the longest durations, with good quality first-class instruments and strict maintenance (Wang and Dickinson, 2013). The AmeriFlux network (Novick et al., 2018) measures ecosystem carbon, water, and energy fluxes across America, and has committed to producing and sharing high-quality eddy covariance data. Selected BSRN and AmeriFlux sites are located above a latitude of 45° to ensure that the sites widely cover different areas and surface types. Equation (1) was also used in the site LST calculation as the surface temperature was not directly recorded. BBE was extracted from the GLASS BEE product. All site observations were quality controlled by individual quality marks.

The raw site observations with 1-min temporal resolution were averaged in a 15-min time window that was centered over the daily satellite passing time. In addition, the site observations with half-hour temporal resolution were extracted by pairing the closest records with the satellite passing time. Bias, RMSE, and R^2 were used as validation indices (Jia et al., 2016). Table 2 lists the basic site information.

Table 2. Metadata for each site.

Network	Site ID	Lat (°)	Lon (°)	Biome type	Temporal resolution (min)
SURFRAD	BND	40.052	–88.373	cropland	1
SURFRAD	FPK	48.308	–105.102	grassland	1
SURFRAD	GWN	34.255	–89.873	pastureland	1
SURFRAD	DRA	36.624	–116.019	arid shrubland	1
SURFRAD	PSU	40.720	–77.931	cropland	1
SURFRAD	SXF	43.734	–96.6231	grassland	1
SURFRAD	TBL	40.125	–105.237	grasslands and shrublands	1
AmeriFlux	Ho1	45.204	–68.740	evergreen needleleaf forests	30

AmeriFlux	UMB	45.560	–84.714	deciduous broadleaf forests	30
BSRN	ALE	82.490	–62.420	tundra	1
BSRN	BAR	71.323	–156.607	tundra	1
BSRN	PAY	46.815	6.944	agriculture	1
BSRN	TIK	71.586	128.919	tundra	1
BSRN	TOR	58.254	26.462	grassland	1

3. Results and discussion

3.1 Validation results

Ground measurement validation was essential to evaluate the algorithm accuracy and suitability under different conditions. Figure 3a (3c) illustrates the VIIRS (MYD21) clear-sky LST samples and cloudy-sky LST against paired ground measurements at the 14 sites in 2013. Satellite retrieved, but likely cloud-contaminated samples, were separated from the clear-sky cases and compared with the reconstructed results in Figure 3b and d. The input for MYD21 was the same as that for VIIRS while the instantaneous DSR was converted from the VIIRS to the MYD passing time.

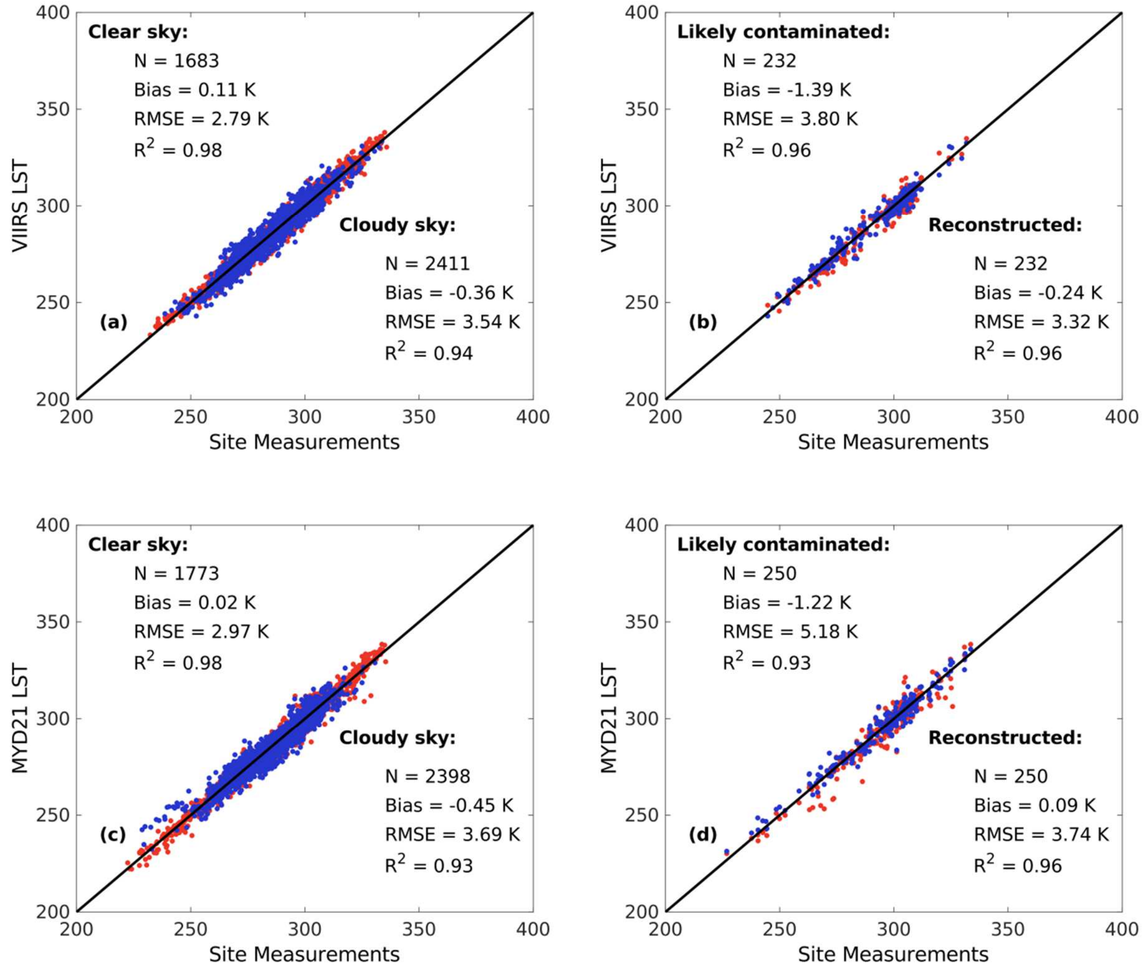

Figure 3. Validation of all-sky land surface temperature (LST) at the 14 sites: (a) VIIRS clear-sky and cloudy-sky samples, (b) VIIRS likely cloud-contaminated and corresponding reconstructed samples, (c) same as (a), but for MYD21, and (d) same as (b), but for MYD21. Red samples are the retrieval results while blue samples are those recovered in this study.

The overall RMSE of the estimated cloudy-sky LST of VIIRS was 3.54 K with a bias of –0.36 K and R^2 of 0.94 (N = 2,411) based on the ground measurements from the 14 sites in 2013; this is slightly larger than the high-quality clear-sky LST retrieval accuracy (Figure 3a), but better than the likely contaminated retrieval results (Figure 3b). The VIIRS likely contaminated samples had a larger RMSE of 3.80 K with a bias of –1.39 K (Figure 3b), as compared with the clear-sky samples (Figure 3a). However, after reconstruction, the results were bias-corrected (–0.24 K) with an improved RMSE (3.32 K). The validation over the 14 sites demonstrated that the method can precisely estimate the cloudy-sky LST and reconstruct the clear-sky LST contaminated by clouds over different land cover types. By comparison, the cloudy-sky LST estimated from MYD21 also resulted in a similar accuracy (RMSE = 3.69 K) in relation to the VIIRS results, indicating that the method is sensor independent and can be used in similar polar-orbiting satellite products. In addition, the negative bias and larger RMSE of the likely contaminated clear-sky MYD21 LST were also corrected (Figure 3d).

Table 3 summarizes the individual validation statistics of the cloudy-sky LST. The cloudy-sky LST estimated from the AMSR2 PMW is also included in Table 3 for comparison.

Table 3. Validation statistics for the cloudy-sky land surface temperature (LST) at the 14 sites in 2013 (Unit: K).

	VIIRS			**MYD21**			**AMSR2**		
	Bias	RMSE	R^2	Bias	RMSE	R^2	Bias	RMSE	R^2
BND	–0.46	2.86	0.94	–0.56	3.05	0.94	0.17	4.68	0.85
FPK	–1.04	4.11	0.94	–1.36	4.15	0.94	1.43	4.44	0.91
GWN	–0.52	2.56	0.93	0.28	2.88	0.93	–2.08	4.38	0.84
DRA	0.54	3.90	0.93	–0.75	4.13	0.91	–2.37	5.51	0.89
PSU	0.11	2.71	0.95	–0.32	2.61	0.94	–1.22	2.87	0.95
SXF	–0.02	2.78	0.96	–0.79	3.26	0.94	0.40	4.10	0.91
TBL	–0.70	4.91	0.89	0.42	5.41	0.86	–2.51	4.98	0.91
Ho1	0.31	2.81	0.94	0.21	2.80	0.94	0.05	3.53	0.91

UMB	1.00	4.33	0.88	–0.24	4.08	0.86	0.22	4.55	0.88
ALE	–0.17	3.38	0.89	0.21	3.91	0.88	–1.67	5.52	0.87
BAR	–1.25	3.65	0.86	–1.11	3.65	0.80	–0.45	6.36	0.66
PAY	0.22	3.91	0.84	–0.61	3.58	0.86	0.67	4.02	0.81
TIK	–1.92	4.48	0.94	0.11	5.68	0.92	–1.76	5.09	0.93
TOR	–1.69	3.00	0.96	–1.44	2.52	0.97	–0.08	4.82	0.86

Based on the validation statistics, the cloudy-sky LST accuracy of the VIIRS simultaneous retrieval varied from 2.56 to 4.91 K over the 14 sites and the standard deviation of the RMSE was 0.76 K. In addition, the accuracy of the MYD21 cloudy-sky LST had a similar accuracy in the range from 2.61 to 5.68 K. The largest RMSE of the VIIRS results was at the TBL site, and the temporal variation in Figure 4g indicates that the LST at TBL had a considerably larger variation magnitude on neighboring days, especially in the winter and spring, which was difficult to predict. The cloudy-sky LST estimated from the AMSR2 PMW using the Four-Channel Algorithm was downscaled, resulting in an overall lower accuracy of 4.47 K with a bias of –0.45 K and R^2 of 0.89. The individual site accuracy varied from 2.87 to 6.36 K with a standard deviation of 0.87 K. The validation statistics of the 14 sites suggest that the revised SEB-based cloudy-sky method shows better accuracy and stability than the Four-Channel PMW estimation method.

Zeng et al. (2018) also developed an SEB-based cloudy-sky LST estimation method; vegetation indices were used as reference data to search neighboring similar pixels for reconstructing the hypothetical clear-sky LST for cloudy days. The individual accuracy assessed by the Mean Bias Error (MBE) at six SURFRAD sites (PSU not included) varied from 3.65 to

6.69 K in 2010. We also calculated the MAE for the VIIRS in this study, where the individual accuracy at the six sites varied from 1.89 to 3.85 K. We inferred that simply borrowing the information from spatially neighboring pixels based on the vegetation indices may not be accurate for reconstruction during non-growing seasons. Additionally, spatially neighboring pixels are not usually available for short distances. Directly referring pixels from neighboring clear-sky days usually overlooks the weather disturbance because clear-sky LST changes considerably on a daily basis in comparison with the accuracy requirement, even if the neighboring days are all cloud-free. By comparison, the reanalysis modeling can provide such variation, thus improving the accuracy.

Our method was more accurate and stable at different sites, indicating that it significantly improved upon the accuracy of previous SEB-based cloudy-sky LST estimation methods. To demonstrate the temporal continuity at each site, Figure 4 shows the temporal variations in the all-sky VIIRS LST and site measurements.

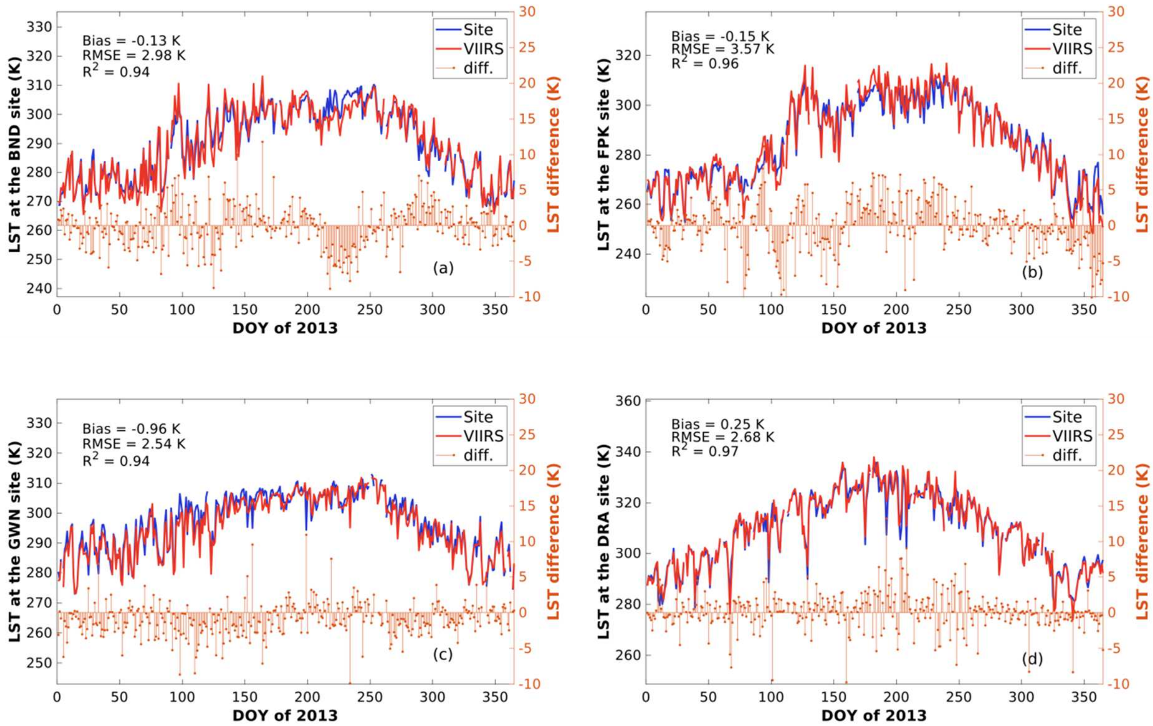

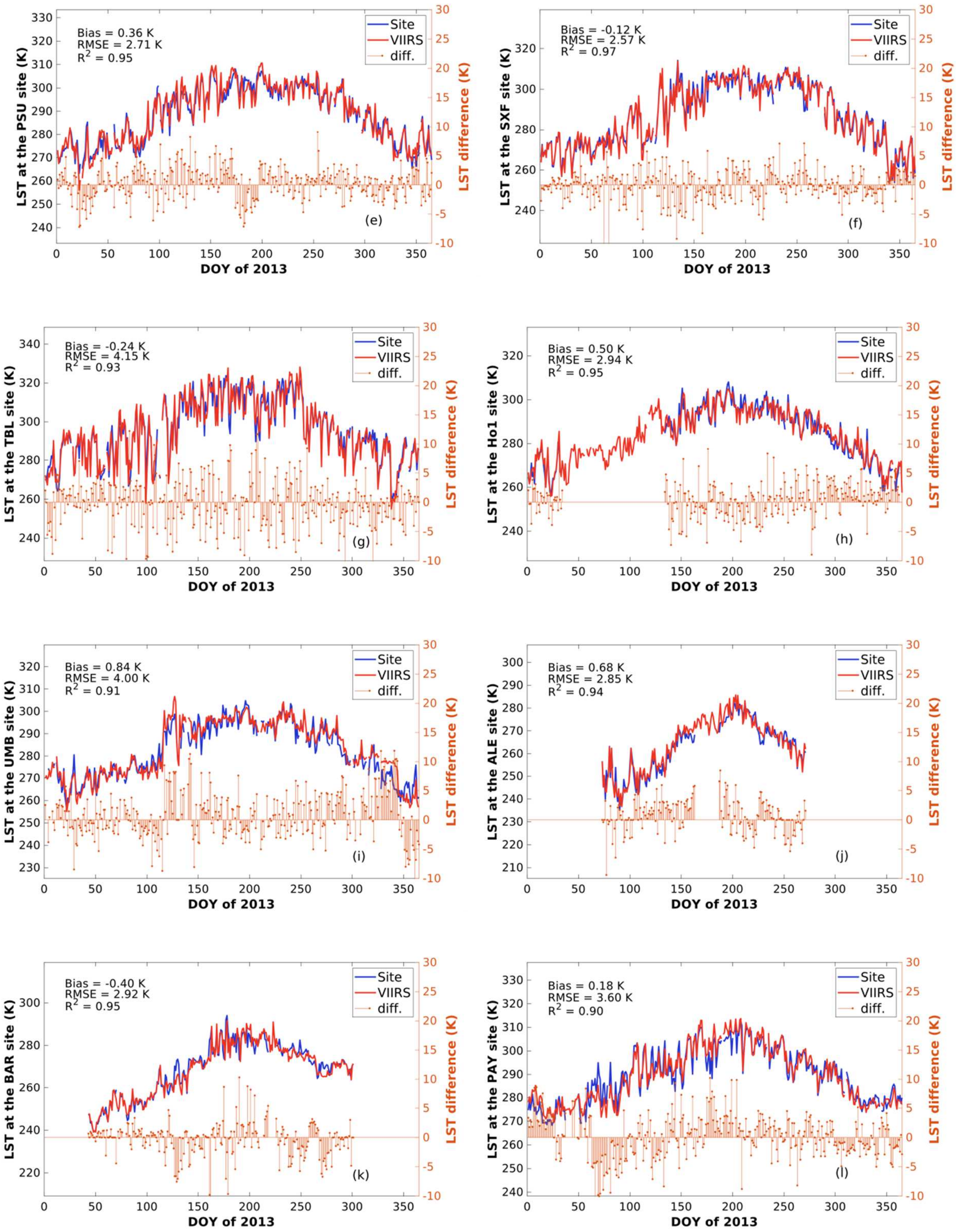

Bias = 0.36 K
RMSE = 2.71 K
R^2 = 0.95
Site
VIIRS
diff.
(e)
LST at the PSU site (K)
LST difference (K)
DOY of 2013
Bias = -0.12 K
RMSE = 2.57 K
R^2 = 0.97
(f)
LST at the SXF site (K)
Bias = -0.24 K
RMSE = 4.15 K
R^2 = 0.93
(g)
LST at the TBL site (K)
Bias = 0.50 K
RMSE = 2.94 K
R^2 = 0.95
(h)
LST at the Ho1 site (K)
Bias = 0.84 K
RMSE = 4.00 K
R^2 = 0.91
(i)
LST at the UMB site (K)
Bias = 0.68 K
RMSE = 2.85 K
R^2 = 0.94
(j)
LST at the ALE site (K)
Bias = -0.40 K
RMSE = 2.92 K
R^2 = 0.95
(k)
LST at the BAR site (K)
Bias = 0.18 K
RMSE = 3.60 K
R^2 = 0.90
(l)
LST at the PAY site (K)

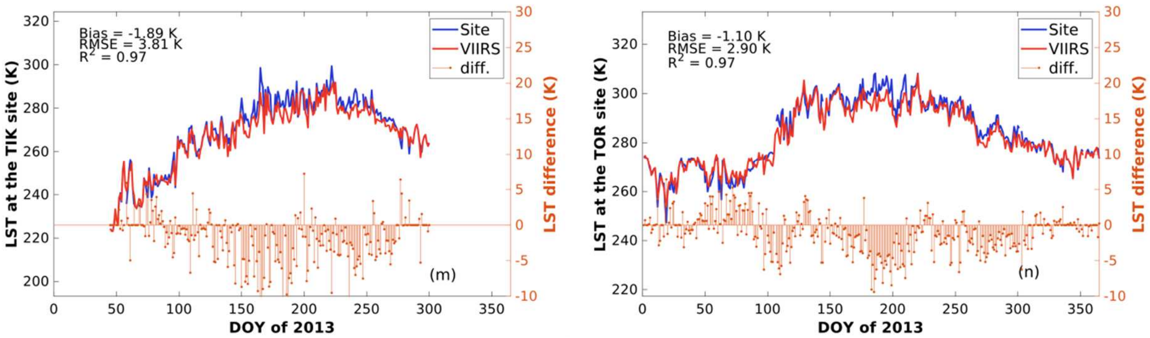

Figure 4. Temporal variations in the all-sky land surface temperature (LST) from the Visible Infrared Imaging Radiometer Suite (VIIRS) and site measurements. The difference for each day is marked by the stem plots using the right y-axis.

By combining the retrieved VIIRS clear-sky LST with the estimated cloudy-sky LST from this study, we can observe that the resulting all-sky LST has no sudden abruptions or discontinuities, and it can capture not only the general LST variation in a year, but also the realistic variabilities (Figure 4g). The accuracy of the all-sky LST varied from 2.54 to 4.15 K at the 14 sites without a clear bias. Comparisons during the polar nights were not shown in Figure 4; this study mainly focused on daytime cloudy-sky LST recovery. Figure 4g illustrates that the LST at TBL had a considerably larger variation magnitude on neighboring days, especially in the winter and spring, which was difficult to predict, causing higher errors at the TBL site (Table 3).

3.2 All-sky LST mapping

VIIRS all-sky LST mapping was processed (Figure 5) for 2018 when the new MCD18 DSR product became recently available (MCD18 will fully be accessible since 2000 in 2021); other auxiliary data were mainly derived from the GLASS satellite products. Eleven VNP21 tiles, which cover the CONUS, were used. Therefore, we focused on the LST pattern by comparing it with the PMW LST. For analysis, we randomly selected two days of LST patterns, one in the winter (February 23) and the other in the summer (July 15).

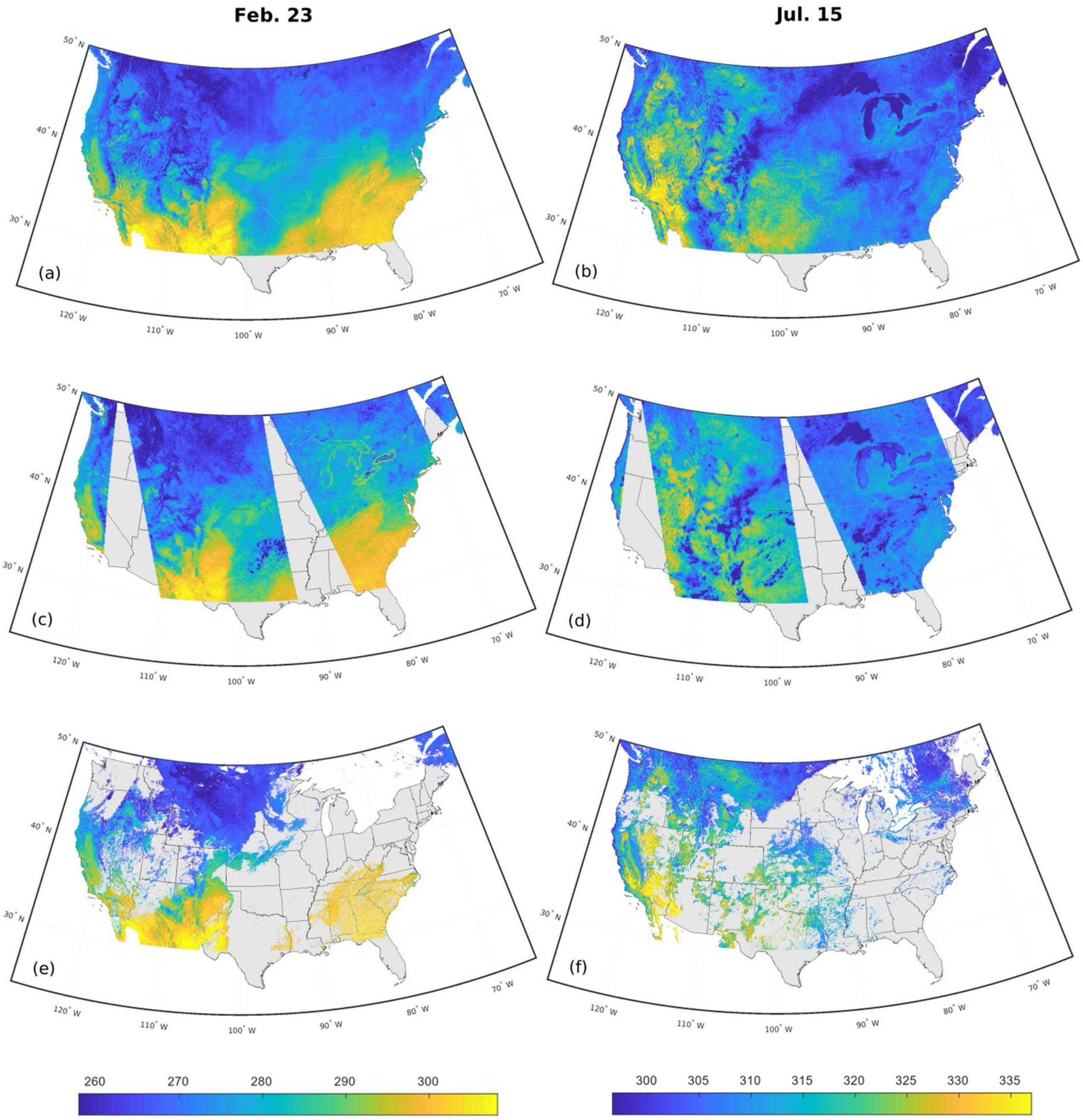

Figure 5. (a, b) Maps of the 1-km all-weather land surface temperature (LST), (c, d) 10-km passive microwave (PMW) LST, and (e, f) the original 1-km Visible Infrared Imaging Radiometer Suite (VIIRS) LST on February 23 and July 15, 2018.

Our results confirm that the proposed method can recover 1-km all-sky LST (Figure 5a and 5b) without spatial discontinuities. The PMW LST can also generate all-sky LST maps, but it has swath gaps and coarser spatial resolution (10 km; Figure 5c and d). The official VNP21 LST, shown for reference (Figure 5e and f), was contaminated by clouds. Using the proposed method, invalid and abnormal retrieved pixels affected by clouds over large areas were recovered (Figure 5a and b) and the overall pattern matched the PMW LST (Figure 5c and d). As the basic input data, except for the clear-sky LST product, are spatially continuous, the proposed method can theoretically provide a spatiotemporal continuous map. Moreover, it does not require spatial or temporal windows for searching reference pixels, and the computation efficiency was improved compared to that reported in previous studies (Yang et al., 2019; Zeng et al., 2018). For the accuracy of the PMW LST, we did not consider the PMW LST as ground truth and only employed it to characterize the overall LST spatial pattern for comparison between seasons.

3.3 Sensitivity analysis

As the proposed physical method required several satellite products as inputs and the estimation of intermediate parameters, a sensitivity analysis was implemented at the 14 sites to characterize the impact and corresponding importance of each input data. Random +/− noises were added into each input data separately to increase the relative errors; the changes in the validation statistics are shown in Figure 6.

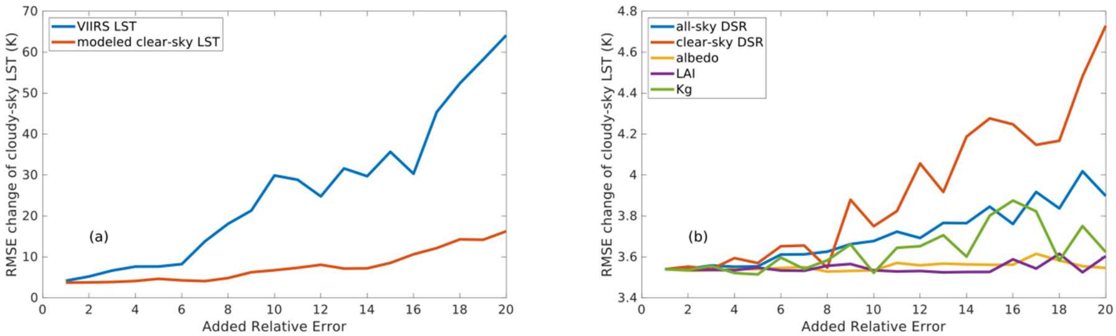

Figure 6. Root mean square error (RMSE) changes when separately adding noise to the basic input data for the (a) input data used in the clear-sky LST reconstruction and (b) input data used in the cloud effect calculation.

As shown in Figure 6a and b, the input variable that leads to the highest sensitivity is the clear-sky LST. This is reasonable because it determines the accuracy of the reconstructed LST for the cloudy days, and the noise is added directly into the final cloudy-sky LST based on Equation 11. The modeled clear-sky LST series is the input data with the second highest impact. In Figure 6b, the clear-sky DSR from the interpolated CERES product is the key variable in the cloud effect calculation while the other important input data is the all-sky DSR from the simultaneous retrieval. This is because these two variables dominate the daytime R_n that highly affect the cloud effect on the ground heat and surface temperature. They play similar roles in the SEB method while the clear-sky DSR shows higher disturbance. This is because the magnitude of the clear-sky DSR is larger than the all-sky DSR on cloudy days, and more absolute errors are added in each error test. The clear-sky DSR usually has stable spatiotemporal variation and smaller relative retrieval uncertainty in the practical application.

We also calculated an overall RMSE of 4.20 K for the LST without cloud effect correction at the 14 sites, which indicates that for those cloudy days, the cloud effect correction reduced the error by approximately 0.66 K after reconstructing the clear-sky LST. The averaged cloud effect at the 14 sites was –1.78 K with a standard deviation of 2.32 K, indicating that the cloud cooling effect on the LST cannot be neglected. The air temperature and total column water vapor were also analyzed, which are not shown in Figure 6b because the superposed data errors had similar influences on both the all-sky R_n and clear-sky R_n while the cloud radiative effect, calculated by the difference in the R_n at different sky conditions, was not impacted by such an increase in the error. Sensitivity analysis revealed that the clear-sky LST reconstruction is the most vital step in the proposed method; our method, using a dynamic model generated from reanalysis with data assimilation, is innovative and robust over different land cover types.

As the clear-sky LST reconstruction is the most vital step in our approach, we compared it with three schemes to confirm that KF assimilation with the ERA5 data was the best choice to reconstruct the hypothetical clear-sky LST for cloudy days. Table 4 summarizes the validation statistics for the three schemes (reference data + fusion method: clear-sky LST climatology + KF, CERES clear-sky LST + KF, and ERA5 clear-sky LST + linear regression). The CERES clear-sky LST series was computed from the clear-sky DLW and ULW series released from the CERES SYN1deg-1hour clear-sky surface radiation product. Both the LST series from CERES and ERA5 were downscaled by DEM and LAI before generating the dynamic models.

Table 4. Validation statistics for the cloudy-sky land surface temperature (LST) from different schemes at the 14 sites in 2013 (Unit: K).

	climatology + KF			**CERES + KF**			**ERA5 + Linear Regression**		
	Bias	RMSE	R^2	Bias	RMSE	R^2	Bias	RMSE	R^2
BND	–0.50	5.41	0.81	–0.95	3.89	0.90	–0.53	2.67	0.95

FPK	–0.26	7.56	0.77	0.12	4.50	0.92	1.20	4.13	0.93
GWN	–0.21	5.91	0.65	–1.53	3.47	0.89	–0.30	2.91	0.94
DRA	–0.37	4.48	0.91	–1.83	5.20	0.84	0.28	3.80	0.93
PSU	1.15	6.10	0.80	–0.15	3.12	0.94	1.37	3.07	0.95
SXF	0.56	6.20	0.82	0.28	3.82	0.82	1.26	3.41	0.95
TBL	0.84	7.89	0.73	–1.55	7.01	0.80	–0.91	5.55	0.85
Ho1	–0.33	5.62	0.80	–0.13	3.17	0.92	0.20	2.73	0.94
UMB	–1.51	7.41	0.74	0.86	5.36	0.84	1.39	5.42	0.79
ALE	0.94	5.30	0.75	0.53	3.43	0.88	–1.92	5.09	0.76
BAR	–1.10	5.01	0.68	–0.15	3.96	0.80	–1.65	4.41	0.82
PAY	2.49	6.23	0.72	0.55	4.48	0.79	2.48	4.81	0.84
TIK	0.57	6.59	0.88	1.51	4.04	0.92	–2.67	5.15	0.94
TOR	–2.57	6.05	0.82	–1.32	2.96	0.95	–1.23	2.56	0.98
Total	–0.39	6.48	0.81	–0.37	4.40	0.90	0.31	4.05	0.91

First, we generated the clear-sky LST climatology at the 14 sites using the MYD21 from 2005 to 2019. This method was also used for LAI retrieval (Xiao et al., 2011); however, the overall validation accuracy was 6.48 K, which was significantly lower than the results of this study. We infer that this was because the LST variation from day to day is large compared with the accuracy requirement while the LAI changes slowly within a few days. For example, the best site for this scheme was DRA, which had a smooth LST variation over one year, except for several cloudy days (Figure 4d). In this area, the weather condition was sunny and dry with approximately 278 clear-sky days in 2013; this number was higher at other sites. Therefore, it was easier to predict the LST variation based on the climatology series. In contrast, reconstructing the missing LST at site TBL was difficult, which has a considerably larger LST variation. Moreover, the land cover type is more varied; the LST for the sites covered by crops is more difficult to predict based on climatology, as the crop type may change from year to year, such as the PSU site.

We also designed a scheme using CERES because it provides a clear-sky longwave radiation series based on satellite observations, which can be used for building a clear-sky LST dynamic model. The results showed that the cloudy-sky LST estimated by CERES had an RMSE of 4.40 K. We inferred that the performance of the parametrization scheme for the CERES Goddard Earth Observing System (GEOS-5.4.1) Data Assimilation System (Doelling et al., 2016) may be inferior in terms of predicting the clear-sky longwave radiation compared to that of the ERA5. The first two schemes suggest that the ERA5 is the best reference data to reconstruct clear-sky LST.

Linear regression was employed to replace the KF to correct the ERA5 clear-sky series. The linear regression was processed using all clear-sky samples and applied to cloudy days, followed by the superposition of the cloud effect. The validation results of scheme 3 showed that this scheme had a higher RMSE (4.05 K) than the KF scheme used in this study. Scheme 3 demonstrates that the KF was more suitable for calibrating the clear-sky LST series from the ERA5.

In summary, the sensitivity analysis indicated that the clear-sky LST reconstruction controls the accuracy of the cloudy-sky LST; ERA5 provides more reliable prediction information for LST construction while the KF algorithm is the best solution for calibrating the modeled clear-sky LST series. In practical applications, the dynamic model does not have to be the annual temporal profile, as long as the modeled clear-sky LST series and satellite LST product continue to update, the reconstruction can work efficiently. In addition, the proposed method does not require spatiotemporal window searching, which increases the computational efficiency. Therefore, the proposed scheme can be easily utilized in real-time all-sky LST production.

4. Conclusions

Thermal remote sensing plays a vital role in regularly monitoring LST at regional to global scales. However, clouds in the atmosphere greatly limit this capability because only clear-sky LST can be estimated from TIR observations. In this study, we presented an SEB method to estimate the cloudy-sky LST from polar-orbiting satellite observations. By assimilating clear-sky satellite LST estimates using the simultaneous retrieval algorithm into a time-evolving model built using the ERA5 reanalysis data, the hypothetical clear-sky LST was reconstructed for those cloudy pixels. The cloudy-sky LST was then estimated by superposing cloud effects to the reconstructed clear-sky LST based on SEB theory.

This method was validated using in situ measurements at 14 sites from SURFRAD, BSRN, and AmeriFlux during 2013; the overall RMSE of the estimated cloudy-sky LST from VIIRS data was 3.54 K with a bias of −0.36 K and R^2 of 0.94 (N = 2411), which was slightly lower than the accuracy of the high-quality clear-sky LST retrieval results, but was better than the likely cloud-contaminated retrieval. The samples fell along the 1:1 line for both the low- and high- value zones at different sites, indicating that the method can be used in different seasons and with various land cover types. By separating the retrieved, but likely cloud-contaminated samples (N = 232), we also found that our reconstruction method improved the accuracy from

3.80 to 3.32 K, and the negative bias (–1.39 K) was corrected to –0.24 K. The proposed method also worked for MODIS LST estimations, which exhibited an RMSE of 3.69 K, a bias of −0.45 K, and R^2 of 0.93. Validation statistics demonstrated that the proposed method had better accuracy than the downscaled cloudy-sky LST estimated from the AMSR2 PMW data. The temporal variation in the reconstructed all-sky LST revealed that the estimated LST was temporally continuous and matched ground-based site measurements. The accuracies of the all-sky LST varied from 2.54 to 4.15 K at the 14 sites. The validation results indicated that the proposed SEB-based physical method was generic for different polar-orbiting satellite LST retrievals (e.g., MODIS and VIIRS) and could estimate the LST under cloudy-sky conditions in the daytime. It could also correct the cloud contamination for clear-sky retrieved cases. Moreover, it could be combined with a simultaneous retrieval algorithm with physical consistency.

The proposed method can be potentially implemented globally to generate real-time spatially continuous maps with good spatial resolution. We evaluated the spatial patterns of the estimated LST results from VNP21 on February 23 and July 15, 2018, over the CONUS, which were compared with the AMSR2 PMW LST and the originally released LST from VNP21. The results revealed that this method was able to reconstruct the contaminated LST values, fill the pixels covered by clouds over large areas, and efficiently match the spatial pattern of the PMW LST both in winter and summer. The imagery results had more spatial details than those of the PMW LST, as the spatial resolution was significantly higher than the PWW observations.

Sensitivity analysis was conducted to investigate the importance of the input data in the physical method. The clear-sky LST, to be assimilated in the dynamic model, was the most important input for the cloudy-sky LST estimation. Large errors in the DSR also affected the cloud effect correction. However, the estimated LST was less sensitive to the soil thermal conductivity and LAI. We also calculated an overall RMSE of 4.20 K for the LST without cloud effect correction; in other words, the cloud effect correction reduced the error by ~0.66 K. Comparatively, the clear-sky LST reconstruction controlled the ultimate accuracy because its error was directly inherited by the cloudy-sky LST. The proposed method provides an innovative approach to process this step. Finally, a comparison of three schemes demonstrated that calibrating the ERA5 clear-sky LST using the KF is the best solution for reconstructing the hypothetical clear-sky LST for cloudy days.

By assimilating the retrieved LST from remote sensing data to a time-evolving model built by reanalysis data, we proposed a generic cloudy-sky LST estimation method for polar-orbiting satellites. This method has the potential to be efficiently applied for global real-time production without gaps. This is a development of the simultaneous retrieval algorithm, which can maintain the all-sky LST and other outputs, such as the DSR, albedo, and LAI, with physical consistency. In the future, we intend to apply this method to geostationary satellite LST products, at which point continuous LST series data will be used to generate all-sky evapotranspiration and sensible heat datasets.

Acknowledgments

This study was partially supported by the National Key Research and Development Program of China (No. 2016YFA0600103). The authors gratefully acknowledge the ECMWF center for providing ERA5 reanalysis data (https://www.ecmwf.int/). We also thank the CERES science team, the VNP21 and MYD21 science team, and the GLASS science team for providing satellite products. MODIS and VIIRS products can be downloaded from Earth Data (https://earthdata.nasa.gov); CERES products can be accessed from its official website (https://ceres.larc.nasa.gov/); GMTED2010 DEM product can be accessed at (https://topotools.cr.usgs.gov/gmted_viewer/gmted2010_global_grids.php); and GLASS products can be downloaded from the UMD GLASS website (http://glass.umd.edu/). We would also like to thank JAXA for providing AMSR2 data (https://gcom-w1.jaxa.jp/). This study used in situ measurements acquired by the SURFRAD community (https://www.esrl.noaa.gov/gmd/grad/surfrad/), BSRN (https://bsrn.awi.de/), and AmeriFlux (https://ameriflux.lbl.gov/). We also thank Ji Zhou, Xiangchen Meng, Shugui Zhou, Xiaodong Zhang, and Jin Ma for discussion and technical consultation.

Author contributions

S. Liang conceived the scope of the research. A. Jia and H. Ma processed the data. A. Jia, S. Liang, and D. Wang performed the interpretation of the results. A. Jia and S. Liang wrote the manuscript. All authors contributed to article revision.

References

Arboleda, A., Ghilain, N., & Gellens-Meulenberghs, F. (2017). Continuous monitoring of evapotranspiration (ET) overview of LSA-SAF evapotranspiration products. *Remote Sensing for Agriculture, Ecosystems, and Hydrology Xix, 10421*

Augustine, J.A., DeLuisi, J.J., & Long, C.N. (2000). SURFRAD - A national surface radiation budget network for atmospheric research. *Bulletin of the American Meteorological Society, 81*, 2341-2357

Bishop, G., & Welch, G. (2001). An introduction to the kalman filter. *Proc of SIGGRAPH, Course, 8*, 41

CERES_Team (2013). CERES_SYN1deg_Ed3A Data_Quality_Summary. *CERES Offical Website http://ceres.larc.nasa.gov/documents/DQ_summaries/CERES_SYN1deg_Ed3A_DQS.pdf*

Chen, J.M., & Liu, J. (2020). Evolution of evapotranspiration models using thermal and shortwave remote sensing data. *Remote Sensing of Environment, 237*, 111594

Chen, S.-s., Chen, X.-z., Chen, W.-q., Su, Y.-x., & Li, D. (2011). A simple retrieval method of land surface temperature from AMSR-E passive microwave data—A case study over Southern China during the strong snow disaster of 2008. *International journal of applied earth observation and geoinformation, 13*, 140-151

Cheng, J., Liang, S., Verhoef, W., Shi, L., & Liu, Q. (2015). Estimating the hemispherical broadband longwave emissivity of global vegetated surfaces using a radiative transfer model. *IEEE Transactions on Geoscience and Remote Sensing, 54*, 905-917

Das, M., & Ghosh, S.K. (2017). A deep-learning-based forecasting ensemble to predict missing data for remote sensing analysis. *IEEE Journal of Selected Topics in Applied Earth Observations and Remote Sensing, 10*, 5228-5236

Dash, P., Göttsche, F.-M., Olesen, F.-S., & Fischer, H. (2002). Land surface temperature and emissivity estimation from passive sensor data: Theory and practice-current trends. *International Journal of remote sensing, 23*, 2563-2594

Doelling, D.R., Sun, M., Nguyen, L.T., Nordeen, M.L., Haney, C.O., Keyes, D.F., & Mlynczak, P.E. (2016). Advances in geostationary-derived longwave fluxes for the CERES synoptic (SYN1deg) product. *Journal of Atmospheric and Oceanic Technology, 33*, 503-521

Duan, S.B., Li, Z.L., & Leng, P. (2017). A framework for the retrieval of all-weather land surface temperature at a high spatial resolution from polar-orbiting thermal infrared and passive microwave data. *Remote Sensing of Environment, 195*, 107-117

Fily, M., Royer, A., Goıta, K., & Prigent, C. (2003). A simple retrieval method for land surface temperature and fraction of water surface determination from satellite microwave brightness temperatures in sub-arctic areas. *Remote Sensing of Environment, 85*, 328-338

Fu, P., Xie, Y., Weng, Q., Myint, S., Meacham-Hensold, K., & Bernacchi, C. (2019). A physical model-based method for retrieving urban land surface temperatures under cloudy conditions. *Remote Sensing of Environment, 230*, 111191

Fu, Q., Liou, K., Cribb, M., Charlock, T., & Grossman, A. (1997). Multiple scattering parameterization in thermal infrared radiative transfer. *Journal of the Atmospheric Sciences, 54*, 2799-2812

Galantowicz, J.F., Moncet, J.L., Liang, P., Lipton, A.E., Uymin, G., Prigent, C., & Grassotti, C. (2011). Subsurface emission effects in AMSR‐E measurements: Implications for land surface microwave emissivity retrieval. *Journal of Geophysical Research: Atmospheres, 116*

Gao, H., Fu, R., Dickinson, R.E., & Juárez, R.I.N. (2007). A practical method for retrieving land surface temperature from AMSR-E over the amazon forest. *IEEE Transactions on Geoscience and Remote Sensing, 46*, 193-199

Hansen, J., Ruedy, R., Sato, M., & Lo, K. (2010). Global surface temperature change. *Reviews of Geophysics, 48*

Hersbach, H., Bell, B., Berrisford, P., Hirahara, S., Horanyi, A., Munoz-Sabater, J., Nicolas, J., Peubey, C., Radu, R., Schepers, D., Simmons, A., Soci, C., Abdalla, S., Abellan, X., Balsamo, G., Bechtold, P., Biavati, G., Bidlot, J., Bonavita, M., De Chiara, G., Dahlgren, P., Dee, D., Diamantakis, M., Dragani, R., Flemming, J., Forbes, R., Fuentes, M., Geer, A., Haimberger, L., Healy, S., Hogan, R.J., Holm, E., Janiskova, M., Keeley, S., Laloyaux, P., Lopez, P., Lupu, C., Radnoti, G., de Rosnay, P., Rozum, I., Vamborg, F., Villaume, S., & Thepaut, J.N. (2020). The ERA5 global reanalysis. *Quarterly Journal of the royal meteorological society, 146*, 1999-2049

Holmes, T., De Jeu, R., Owe, M., & Dolman, A. (2009). Land surface temperature from Ka band (37 GHz) passive microwave observations. *Journal of Geophysical Research: Atmospheres, 114*

Hulley, G., Malakar, N., & Freepartner, R. (2016). Moderate Resolution Imaging Spectroradiometer (MODIS) Land Surface Temperature and Emissivity Product (MxD21) Algorithm Theoretical Basis Document Collection-6. *JPL Publication*, 12-17

Imaoka, K., Kachi, M., Kasahara, M., Ito, N., Nakagawa, K., & Oki, T. (2010). Instrument performance and calibration of AMSR-E and AMSR2. *International Archives of the Photogrammetry, Remote Sensing and Spatial Information Science, 38*, 13-18

Islam, T., Hulley, G.C., Malakar, N.K., Radocinski, R.G., Guillevic, P.C., & Hook, S.J. (2016). A physics-based algorithm for the simultaneous retrieval of land surface temperature and emissivity from VIIRS thermal infrared data. *IEEE Transactions on Geoscience and Remote Sensing, 55*, 563-576

Jia, A., Jiang, B., Liang, S., Zhang, X., & Ma, H. (2016). Validation and Spatiotemporal Analysis of CERES Surface Net Radiation Product. *Remote Sensing, 8*, 90

Jia, A., Liang, S., Jiang, B., Zhang, X., & Wang, G. (2018). Comprehensive assessment of global surface net radiation products and uncertainty analysis. *Journal of Geophysical Research: Atmospheres, 123*, 1970-1989

Jia, A.L., Liang, S.L., Wang, D.D., Jiang, B., & Zhang, X.T. (2020). Air pollution slows down surface warming over the Tibetan Plateau. *Atmospheric Chemistry and Physics, 20*, 881-899

Jiang, B., Liang, S., Ma, H., Zhang, X., Xiao, Z., Zhao, X., Jia, K., Yao, Y., & Jia, A. (2016). GLASS Daytime All-Wave Net Radiation Product: Algorithm Development and Preliminary Validation. *Remote Sensing, 8*, 222

Jiang, B., Zhang, Y., Liang, S., Wohlfahrt, G., Arain, A., Cescatti, A., Georgiadis, T., Jia, K., Kiely, G., & Lund, M. (2015). Empirical estimation of daytime net radiation from shortwave radiation and ancillary information. *Agricultural & Forest Meteorology, s 211–212*, 23-36

Jin, M. (2000). Interpolation of surface radiative temperature measured from polar orbiting satellites to a diurnal cycle: 2. Cloudy‐pixel treatment. *Journal of Geophysical Research: Atmospheres, 105*, 4061-4076

Jin, M., & Dickinson, R.E. (2000). A generalized algorithm for retrieving cloudy sky skin temperature from satellite thermal infrared radiances. *Journal of Geophysical Research: Atmospheres, 105*, 27037-27047

Kato, S., Rose, F.G., Rutan, D.A., Thorsen, T.J., Loeb, N.G., Doelling, D.R., Huang, X., Smith, W.L., Su, W., & Ham, S.-H. (2018). Surface irradiances of edition 4.0 Clouds and the Earth's

Radiant Energy System (CERES) Energy Balanced and Filled (EBAF) data product. *Journal of Climate, 31*, 4501-4527

Kou, X., Jiang, L., Bo, Y., Yan, S., & Chai, L. (2016). Estimation of land surface temperature through blending MODIS and AMSR-E data with the Bayesian maximum entropy method. *Remote Sensing, 8*, 105

Li, Z.-L., Tang, B.-H., Wu, H., Ren, H., Yan, G., Wan, Z., Trigo, I.F., & Sobrino, J.A. (2013). Satellite-derived land surface temperature: Current status and perspectives. *Remote Sensing of Environment, 131*, 14-37

Liang, S. (2004). *Quantitative Remote Sensing of Land Surfaces*. Wiley-Interscience

Liang, S. (2017). *Remote Sensing of Earth's Energy Budget: An Overview of Recent Progress. In S. Liang (Ed.), Comprehensive Remote Sensing vol. 5: Earth's Energy Budget (p. in press). Oxford, UK: Elsevier.*

Liang, S., Wang, D., He, T., & Yu, Y. (2019). Remote sensing of earth's energy budget: Synthesis and review. *International Journal of Digital Earth, 12*, 737-780

Liang, S., Zhang, X., Xiao, Z., Cheng, J., Liu, Q., & Zhao, X. (2014). *Global LAnd Surface Satellite (GLASS) Products*. Springer International Publishing

Liang, S., Zhao, X., Liu, S., Yuan, W., Cheng, X., Xiao, Z., Zhang, X., Liu, Q., Cheng, J., & Tang, H. (2013). A long-term Global LAnd Surface Satellite (GLASS) data-set for environmental studies. *International Journal of Digital Earth, 6*, 5-33

Liang, S.L., Wang, K.C., Zhang, X.T., & Wild, M. (2010). Review on Estimation of Land Surface Radiation and Energy Budgets From Ground Measurement, Remote Sensing and Model Simulations. *IEEE Journal of Selected Topics in Applied Earth Observations and Remote Sensing, 3*, 225-240

Liu, N., Liu, Q., Wang, L., Liang, S., Wen, J., Qu, Y., & Liu, S. (2013). A statistics-based temporal filter algorithm to map spatiotemporally continuous shortwave albedo from MODIS data. *Hydrology and Earth System Sciences, 17*, 2121

Liu, X., Tang, B.-H., Yan, G., Li, Z.-L., & Liang, S. (2019). Retrieval of global orbit drift corrected land surface temperature from long-term AVHRR data. *Remote Sensing, 11*, 2843

Liu, Y., Hiyama, T., & Yamaguchi, Y. (2006). Scaling of land surface temperature using satellite data: A case examination on ASTER and MODIS products over a heterogeneous terrain area. *Remote Sensing of Environment, 105*, 115-128

Loeb, N.G., Doelling, D.R., Wang, H.L., Su, W.Y., Nguyen, C., Corbett, J.G., Liang, L.S., Mitrescu, C., Rose, F.G., & Kato, S. (2018). Clouds and the Earth's Radiant Energy System (CERES) Energy Balanced and Filled (EBAF) Top-of-Atmosphere (TOA) Edition-4.0 Data Product. *Journal of Climate, 31*, 895-918

Long, D., Yan, L., Bai, L., Zhang, C., Li, X., Lei, H., Yang, H., Tian, F., Zeng, C., Meng, X., & Shi, C. (2020). Generation of MODIS-like land surface temperatures under all-weather conditions based on a data fusion approach. *Remote Sensing of Environment, 246*, 111863

Lu, L., Venus, V., Skidmore, A., Wang, T., & Luo, G. (2011). Estimating land-surface temperature under clouds using MSG/SEVIRI observations. *International journal of applied earth observation and geoinformation, 13*, 265-276

Luyssaert, S., Jammet, M., Stoy, P.C., Estel, S., Pongratz, J., Ceschia, E., Churkina, G., Don, A., Erb, K., & Ferlicoq, M. (2014). Land management and land-cover change have impacts of similar magnitude on surface temperature. *Nature Climate Change, 4*, 389-393

Ma, H., Liang, S., Shi, H., & Zhang, Y. (2020). An Optimization Approach for Estimating Multiple Land Surface and Atmospheric Variables From the Geostationary Advanced Himawari Imager Top-of-Atmosphere Observations. *IEEE Transactions on Geoscience and Remote Sensing*

Ma, H., Liang, S., Xiao, Z., & Shi, H. (2017). Simultaneous inversion of multiple land surface parameters from MODIS optical–thermal observations. *ISPRS Journal of Photogrammetry and Remote Sensing, 128*, 240-254

Ma, H., Liang, S., Xiao, Z., & Wang, D. (2018). Simultaneous Estimation of Multiple Land-Surface Parameters From VIIRS Optical-Thermal Data. *IEEE Geoscience and Remote Sensing Letters, 15*, 156-160

Mao, K., Shi, J., Li, Z., Qin, Z., Li, M., & Xu, B. (2007). A physics-based statistical algorithm for retrieving land surface temperature from AMSR-E passive microwave data. *Science in China Series D: Earth Sciences, 50*, 1115-1120

Minder, J.R., Mote, P.W., & Lundquist, J.D. (2010). Surface temperature lapse rates over complex terrain: Lessons from the Cascade Mountains. *Journal of Geophysical Research: Atmospheres, 115*

Neteler, M. (2010). Estimating daily land surface temperatures in mountainous environments by reconstructed MODIS LST data. *Remote Sensing, 2*, 333-351

Njoku, E.G., & Li, L. (1999). Retrieval of land surface parameters using passive microwave measurements at 6-18 GHz. *IEEE Transactions on Geoscience and Remote Sensing, 37*, 79-93

Nogueira, K., Fadel, S.G., Dourado, Í.C., Werneck, R.d.O., Muñoz, J.A., Penatti, O.A., Calumby, R.T., Li, L.T., dos Santos, J.A., & Torres, R.d.S. (2018). Exploiting ConvNet diversity for flooding identification. *IEEE Geoscience and Remote Sensing Letters, 15*, 1446-1450

Novick, K.A., Biederman, J., Desai, A., Litvak, M., Moore, D.J., Scott, R., & Torn, M. (2018). The AmeriFlux network: A coalition of the willing. *Agricultural and Forest Meteorology, 249*, 444-456

Ohmura, A., Dutton, E.G., Forgan, B., Fröhlich, C., Gilgen, H., Hegner, H., Heimo, A., König-Langlo, G., McArthur, B., & Müller, G. (1998). Baseline Surface Radiation Network (BSRN/WCRP): New precision radiometry for climate research. *Bulletin of the American Meteorological Society, 79*, 2115-2136

Owe, M., & Van De Griend, A. (2001). On the relationship between thermodynamic surface temperature and high-frequency (37 GHz) vertically polarized brightness temperature under semi-arid conditions. *International Journal of remote sensing, 22*, 3521-3532

Rao, Y., Liang, S., Wang, D., Yu, Y., Song, Z., Zhou, Y., Shen, M., & Xu, B. (2019). Estimating daily average surface air temperature using satellite land surface temperature and top-of-atmosphere radiation products over the Tibetan Plateau. *Remote Sensing of Environment, 234*, 111462

Shi, H., Xiao, Z., Liang, S., & Ma, H. (2017). A Method for Consistent Estimation of Multiple Land Surface Parameters From MODIS Top-of-Atmosphere Time Series Data. *IEEE Transactions on Geoscience and Remote Sensing, 55*, 5158-5173

Sobrino, J.A., Jiménez-Muñoz, J.C., & Paolini, L. (2004). Land surface temperature retrieval from LANDSAT TM 5. *Remote Sensing of Environment, 90*, 434-440

Sun, D., & Kafatos, M. (2007). Note on the NDVI‐LST relationship and the use of temperature‐related drought indices over North America. *Geophysical Research Letters, 34*

Sun, D., Li, Y., Zhan, X., Houser, P., Yang, C., Chiu, L., & Yang, R. (2019). Land Surface Temperature Derivation under All Sky Conditions through Integrating AMSR-E/AMSR-2 and MODIS/GOES Observations. *Remote Sensing, 11*, 1704

Tomlinson, C.J., Chapman, L., Thornes, J.E., & Baker, C. (2011). Remote sensing land surface temperature for meteorology and climatology: a review. *Meteorological Applications, 18*, 296-306

Wan, Z. (2006). MODIS land surface temperature products users' guide. *Institute for Computational Earth System Science, University of California, Santa Barbara, CA*, 5-15

Wan, Z.M., & Li, Z.L. (1997). A physics-based algorithm for retrieving land-surface emissivity and temperature from EOS/MODIS data. *IEEE Transactions on Geoscience and Remote Sensing, 35*, 980-996

Wang, D., Liang, S., Zhang, Y., Gao, X., Brown, M.G., & Jia, A. (2020). A New Set of MODIS Land Products (MCD18): Downward Shortwave Radiation and Photosynthetically Active Radiation. *Remote Sensing, 12*, 168

Wang, K., & Dickinson, R.E. (2013). Global atmospheric downward longwave radiation at the surface from ground - based observations, satellite retrievals, and reanalyses. *Reviews of Geophysics, 51*, 150-185

Wang, K., & Liang, S. (2009). Evaluation of ASTER and MODIS land surface temperature and emissivity products using long-term surface longwave radiation observations at SURFRAD sites. *Remote Sensing of Environment, 113*, 1556-1565

Wen, J., Su, Z., & Ma, Y. (2003). Determination of land surface temperature and soil moisture from Tropical Rainfall Measuring Mission/Microwave Imager remote sensing data. *Journal of Geophysical Research: Atmospheres, 108*, ACL 2-1-ACL 2-10

Weng, F., & Grody, N.C. (1998). Physical retrieval of land surface temperature using the special sensor microwave imager. *Journal of Geophysical Research: Atmospheres, 103*, 8839-8848

Westermann, S., Langer, M., & Boike, J. (2011). Spatial and temporal variations of summer surface temperatures of high-arctic tundra on Svalbard—implications for MODIS LST based permafrost monitoring. *Remote Sensing of Environment, 115*, 908-922

Wu, P., Yin, Z., Yang, H., Wu, Y., & Ma, X. (2019). Reconstructing Geostationary Satellite Land Surface Temperature Imagery Based on a Multiscale Feature Connected Convolutional Neural Network. *Remote Sensing, 11*, 300

Xiao, Z., Liang, S., Wang, J., Jiang, B., & Li, X. (2011). Real-time retrieval of Leaf Area Index from MODIS time series data. *Remote Sensing of Environment, 115*, 97-106

Xiao, Z., Liang, S., Wang, J., Xiang, Y., Zhao, X., & Song, J. (2016). Long-time-series global land surface satellite leaf area index product derived from MODIS and AVHRR surface reflectance. *IEEE Transactions on Geoscience and Remote Sensing, 54*, 5301-5318

Xu, S., & Cheng, J. (2021). A new land surface temperature fusion strategy based on cumulative distribution function matching and multiresolution Kalman filtering. *Remote Sensing of Environment, 254*, 112256

Xu, T., He, X., Bateni, S.M., Auligne, T., Liu, S., Xu, Z., Zhou, J., & Mao, K. (2019). Mapping regional turbulent heat fluxes via variational assimilation of land surface temperature data from polar orbiting satellites. *Remote Sensing of Environment, 221*, 444-461

Xu, Y., & Shen, Y. (2013). Reconstruction of the land surface temperature time series using harmonic analysis. *Computers & geosciences, 61*, 126-132

Yang, G., Sun, W., Shen, H., Meng, X., & Li, J. (2019). An Integrated Method for Reconstructing Daily MODIS Land Surface Temperature Data. *IEEE Journal of Selected Topics in Applied Earth Observations and Remote Sensing, 12*, 1026-1040

Yu, W., Ma, M., Wang, X., & Tan, J. (2014). Estimating the land-surface temperature of pixels covered by clouds in MODIS products. *Journal of Applied Remote Sensing, 8*, 083525

Yu, Y., Tarpley, D., Privette, J.L., Goldberg, M.D., Raja, M.R.V., Vinnikov, K.Y., & Xu, H. (2008). Developing algorithm for operational GOES-R land surface temperature product. *IEEE Transactions on Geoscience and Remote Sensing, 47*, 936-951

Yuan, Q., Shen, H., Li, T., Li, Z., Li, S., Jiang, Y., Xu, H., Tan, W., Yang, Q., & Wang, J. (2020). Deep learning in environmental remote sensing: Achievements and challenges. *Remote Sensing of Environment, 241*, 111716

Zeng, C., Long, D., Shen, H., Wu, P., Cui, Y., & Hong, Y. (2018). A two-step framework for reconstructing remotely sensed land surface temperatures contaminated by cloud. *ISPRS Journal of Photogrammetry and Remote Sensing, 141*, 30-45

Zhang, L., Zhang, L., & Du, B. (2016). Deep learning for remote sensing data: A technical tutorial on the state of the art. *IEEE Geoscience and Remote Sensing Magazine, 4*, 22-40

Zhang, Q., Yuan, Q., Zeng, C., Li, X., & Wei, Y. (2018). Missing data reconstruction in remote sensing image with a unified spatial–temporal–spectral deep convolutional neural network. *IEEE Transactions on Geoscience and Remote Sensing, 56*, 4274-4288

Zhang, X., Pang, J., & Li, L. (2015). Estimation of land surface temperature under cloudy skies using combined diurnal solar radiation and surface temperature evolution. *Remote Sensing, 7*, 905-921

Zhang, X., Zhou, J., Gottsche, F.-M., Zhan, W., Liu, S., & Cao, R. (2019a). A Method Based on Temporal Component Decomposition for Estimating 1-km All-Weather Land Surface Temperature by Merging Satellite Thermal Infrared and Passive Microwave Observations. *IEEE Transactions on Geoscience and Remote Sensing, 57*, 4670-4691

Zhang, X., Zhou, J., Göttsche, F.-M., Zhan, W., Liu, S., & Cao, R. (2019b). A method based on temporal component decomposition for estimating 1-km all-weather land surface temperature by merging satellite thermal infrared and passive microwave observations. *IEEE Transactions on Geoscience and Remote Sensing, 57*, 4670-4691

Zhang, X., Zhou, J., Liang, S., Chai, L., Wang, D., & Liu, J. (2020). Estimation of 1-km all-weather remotely sensed land surface temperature based on reconstructed spatial-seamless satellite passive microwave brightness temperature and thermal infrared data. *ISPRS Journal of Photogrammetry and Remote Sensing, 167*, 321-344

Zhang, X., Zhou, J., Liang, S., & Wang, D. (2021). A practical reanalysis data and thermal infrared remote sensing data merging (RTM) method for reconstruction of a 1-km all-weather land surface temperature. *Remote Sensing of Environment, 260*, 112437

Zhao, W., & Duan, S.-B. (2020). Reconstruction of daytime land surface temperatures under cloud-covered conditions using integrated MODIS/Terra land products and MSG geostationary satellite data. *Remote Sensing of Environment, 247*, 111931

Zhou, J., Dai, F., Zhang, X., Zhao, S., & Li, M. (2015). Developing a temporally land cover-based look-up table (TL-LUT) method for estimating land surface temperature based on AMSR-E data over the Chinese landmass. *International journal of applied earth observation and geoinformation, 34*, 35-50

Zhou, J., Liang, S., Cheng, J., Wang, Y., & Ma, J. (2018). The GLASS land surface temperature product. *IEEE Journal of Selected Topics in Applied Earth Observations and Remote Sensing, 12*, 493-507

List of Figure Captions

Figure 1. Flowchart of the proposed cloudy-sky land surface temperature (LST) estimation method, where DLW and ULW are the downward and upward longwave radiation, respectively, BBE is the broadband emissivity, DSR is the downward shortwave radiation, LAI is the leaf area index, and ΔG and ΔLST are the cloud effect on the ground heat and LST, respectively.

Figure 2. Validation of the multivariate adaptive regression spline (MARS) modeled R_n by comparison with the ERA5 R_n in terms of the (a) training accuracy and (b) prediction accuracy.

Figure 3. Validation of all-sky land surface temperatures (LSTs) at the 14 sites: (a) VIIRS clear-sky and cloudy-sky samples, (b) VIIRS likely cloud-contaminated and corresponding reconstructed samples, (c) same as (a), but for MYD21, and (d) same as (b), but for MYD21. Red samples are the retrieval results while blue samples are those recovered in this study.

Figure 4. Temporal variations in the all-sky land surface temperature (LST) from the Visible Infrared Imaging Radiometer Suite (VIIRS) and site measurements. The difference for each day is marked by the stem plots using the right y-axis.

Figure 5. (a, b) Maps of the 1-km all-weather land surface temperature (LST), (c, d) 10-km passive microwave (PMW) LST, and (e, f) the original 1-km Visible Infrared Imaging Radiometer Suite (VIIRS) LST on February 23 and July 15, 2018.

Figure 6. Root mean square error (RMSE) changes when separately adding noise to the basic input data for the (a) input data used in the clear-sky LST reconstruction and (b) input data used in the cloud effect calculation.